

# Thermal Pressure in the Laser Heated Diamond Anvil Cell: A Quantitative Study and Implications for the Density vs. Mineralogy Correlation of the Mantle

Connor Ethan Yen<sup>1</sup>, Quentin Williams<sup>2</sup>, and Martin Kunz<sup>3</sup>

<sup>1</sup>Lawrence Berkeley National Laboratory

<sup>2</sup>UC Santa Cruz

<sup>3</sup>Lawrence Berkeley National Laboratory (DOE)

November 24, 2022

## Abstract

We present the first quantitative measurements of the magnitude and gradient of thermal pressure in a laser heated diamond anvil cell (LHDAC). The observed thermal pressure is strongly localized and follows the distribution of the laser hotspot. The magnitude of the thermal pressure is of the order of the thermodynamic thermal pressure ( $p_{ad}$ ) with gradients between 0.5 – 1.0 GPa/10  $\mu\text{m}$ . This poses constraints on pressure determinations during PVT equation of state measurements when using a LHDAC. We show that an incomplete account of thermal pressure in PVT experiments can lead to distortions of the coveted depth versus mineralogy correlation. However, the ability to spatially resolve thermal pressure in a LHDAC opens avenues to measure thermodynamic derivative properties, which are important for comprehensive thermodynamic descriptions of the interior of planets.

1 Thermal Pressure in the Laser Heated Diamond Anvil Cell: A Quantitative  
2 Study and Implications for the Density vs. Mineralogy Correlation of the  
3 Mantle

4

5 Connor Ethan Yen<sup>1),2)</sup> Quentin Williams<sup>3)</sup> and Martin Kunz<sup>1)</sup>

6

7

8 <sup>1)</sup> Advanced Light Source, Lawrence Berkeley National Lab, 1 Cyclotron Rd, Berkeley CA 94720

9 <sup>2)</sup> Mathematics, University of California, Berkeley, CA 94720

10 <sup>3)</sup> Earth and Planetary Sciences, University of California, Santa Cruz, CA 95064

11

12 **Keypoints:** laser-heated diamond anvil cell, thermal pressure, density – mineralogy correlation

13

14 **Plain Language Summary:**

15 The primary window into the interior of the Earth below ~10 km are earthquake waves that give us a 3-  
16 dimensional elasticity/density image of the planet. In order to translate this into a geological model of  
17 the Earth, we need to know the physical and chemical response of rocks with the composition of the  
18 Earth's interior at increased pressure and temperature. This is achieved by experiments in which  
19 samples are subjected to the high pressure and temperatures of the deep Earth using laser heated  
20 diamond anvil cells. A long standing problem of such experiments is a hard to quantify pressure term  
21 caused by the heating of the sample. This paper quantifies the thermal pressure distribution in a typical  
22 experiment for the first time and explores the effect of its incomplete knowledge on the possible  
23 mineralogical composition of the Earth.

24

25 **Abstract:**

26 We present the first quantitative measurements of the magnitude and gradient of thermal  
27 pressure in a laser heated diamond anvil cell (LHDAC). The observed thermal pressure is strongly  
28 localized and follows the distribution of the laser hotspot. The magnitude of the thermal pressure is of  
29 the order of the thermodynamic thermal pressure ( $\alpha K_T dT$ ) with gradients between 0.5 – 1.0 GPa/10  
30  $\mu\text{m}$ . This poses constraints on pressure determinations during PVT equation of state measurements  
31 when using a LHDAC. We show that an incomplete account of thermal pressure in PVT experiments can  
32 lead to distortions of the coveted depth versus mineralogy correlation. However, the ability to spatially  
33 resolve thermal pressure in a LHDAC opens avenues to measure thermodynamic derivative properties,  
34 which are important for comprehensive thermodynamic descriptions of the interior of planets.

35 

## 1 Introduction

36 Over the past ~ 25 years, laser heated diamond anvil cells have played an important role in  
37 experimentally accessing the conditions of the interior of the Earth and Earth-sized planets (e.g.  
38 *Williams et al.* [1991]; *Guillaume Fiquet et al.* [1998]; *W Mao et al.* [2004]; *Ismailova et al.* [2016];  
39 *Bassett* [2016]). The technique allows experimental simulation of pressures and temperatures relevant  
40 to the interior of the Earth, while allowing in-situ probing of structural and thermo-elastic properties of  
41 samples using a large portion of the electromagnetic spectrum (e.g. *Shen and Mao* [2016]; *Mezouar et*  
42 *al.* [2017]). Despite the maturity of this technique, there persist remarkable discrepancies between  
43 results reported from different experiments (e.g. *Komabayashi and Fei* [2010]), and also between  
44 experiments and theory (e.g. *Dorogokupets et al.* [2015]).

45 From an experimental angle, the sources of discrepancies in a LHDAC experiment are often  
46 associated with difficulties in measuring the pressure and temperature of the sample chamber. A second  
47 source of experimental uncertainty stems from the difficulty in positioning the probe (e.g. an X-ray  
48 beam) at a position of well-defined pressure and temperature within a sample volume with high thermal  
49 gradients ( $\sim 10^4$  K/mm) (e.g. *Panero and Jeanloz* [2001]; *Abby Kavner and Nugent* [2008]) and non-  
50 hydrostatic stress conditions (e.g. *Meng et al.* [1993]). Differences in sample preparation cause  
51 additional elements of limited reproducibility (e.g. *Marquardt and Marquardt* [2012]), as does  
52 unrecognized contamination (e.g. *Morard et al.* [2017]). An additional, and largely experimentally  
53 uncharacterized, contribution to measurement uncertainties in P-V-T experiments is the increase in  
54 pressure during the heating event due to quasi-isochoric conditions and the concomitant pressure  
55 increase and gradients induced by local heating. This effect is commonly referred to as thermal pressure  
56 ( $P_{th}$ ); it is unrecorded in experimental set-ups where pressure is determined before and/or after the  
57 laser-heating event by using, for example, ruby fluorescence spectrometry. The combination of the laser  
58 heated material's finite shear strength and the temperature gradient produced by the focused laser spot  
59 produces a spatial gradient in thermal pressure which again is of the same order as the size of the  
60 probe.

61 The possible role of thermal pressure in laser-heated diamond cell experiments has long been  
62 recognized, but virtually no experiments have been conducted that measured the variation in thermal  
63 pressure *in situ* across a sample. In fact, the treatment of thermal pressure has been examined largely  
64 from a theoretical perspective. *Heinz* [1990] was the first to quantitatively address this issue from such a  
65 theoretical point of view. He estimated a  $P_{th}$  of  $\sim 2 - 10$  GPa for a spherical Gaussian hot spot with  $T_{max} =$   
66 2000 K, a thermal expansivity  $\alpha = 4 \times 10^{-5}/K$ , Poisson's ratio  $\nu = 0.25$ , and Young's modulus  $E = 200$  GPa.  
67 These calculations were done for various ratios of hot-spot to sample size for two scenarios: the case of  
68 a free surface boundary condition (which implies constant pressure at the surface), and the case of a  
69 constant volume. Calculated values for  $P_{th}$  ( $\sim 4$  to 5 GPa) for small hot spot sizes were very similar in  
70 both scenarios, indicating a local nature of  $P_{th}$  with high pressure gradients associated with the laser-  
71 heated spot. This result implies that most of the thermal pressure is maintained via the shear strength of  
72 the heated material, rather than through the constant volume restriction provided by the metal gasket.

73 *Dewaele et al.* [1998] performed finite element modeling – also based on solving the  
74 thermoelastic equations – for a realistic LHDAC model assembly consisting of samples (stishovite and

75 coesite) sandwiched between an argon pressure medium. Their analysis included the effects of the  
76 thermal conductivity of the sample and pressure medium on the temperature distribution, as well as the  
77 effects of the bulk and shear moduli parameterized as Lamé constants. For both coesite and stishovite,  
78 they differentiated between a model with solid and liquid argon as the pressure medium. Their results  
79 for a solid pressure medium compare well with the results cited by *Heinz* [1990] – a thermal pressure  
80 increase of ~30 % of the ‘cold’ pressure. Interestingly, they found only a small dependence of the  
81 thermal pressure on the relative amount of solid argon used as pressure medium. Their second model,  
82 assuming a completely molten pressure medium, reduced the expected thermal pressure by about 50  
83 %. This model approached the free-surface model of *Heinz* [1990].

84 *G Fiquet et al.* [1996], for the first time, reported direct observations of thermal pressure in a  
85 LHDAC while measuring P-V-T data of MgO periclase using a CO<sub>2</sub> laser. *Andrault et al.* [1998]  
86 experimentally determined the pressure increase induced by laser heating in a LHDAC using the phase  
87 transitions in the Mg<sub>2</sub>SiO<sub>4</sub> and SiO<sub>2</sub> systems. They found that the observed increase relative to the  
88 perfectly isochoric ‘thermodynamic’ limit is sample dependent, correlating positively with the product of  
89 the thermal expansion and bulk modulus,  $\alpha K_T$  (in accord with the ideal thermodynamic definition of  
90 thermal pressure as equal to  $\alpha K_T dT$ ), rather than with the shear modulus.

91 In this work, we experimentally quantify the distribution of thermal pressure created in a  
92 diamond anvil cell by a laser focus spot of 30  $\mu\text{m}$  FWHM – a typical diameter of an experimental laser  
93 heating spot – and compare it with previously published models as well as a simple model based on the  
94 assumption of isochoric conditions. We then use an idealized example to quantify the effect of not fully  
95 taking into account the thermal pressure on thermoelastic properties of a mantle-like material  
96 (Mg<sub>0.88</sub>Fe<sub>0.12</sub>SiO<sub>3</sub> bridgmanite) extracted from a LHDAC experiment, and explore the implications for the  
97 resultant inferred mineralogy versus depth correlation.

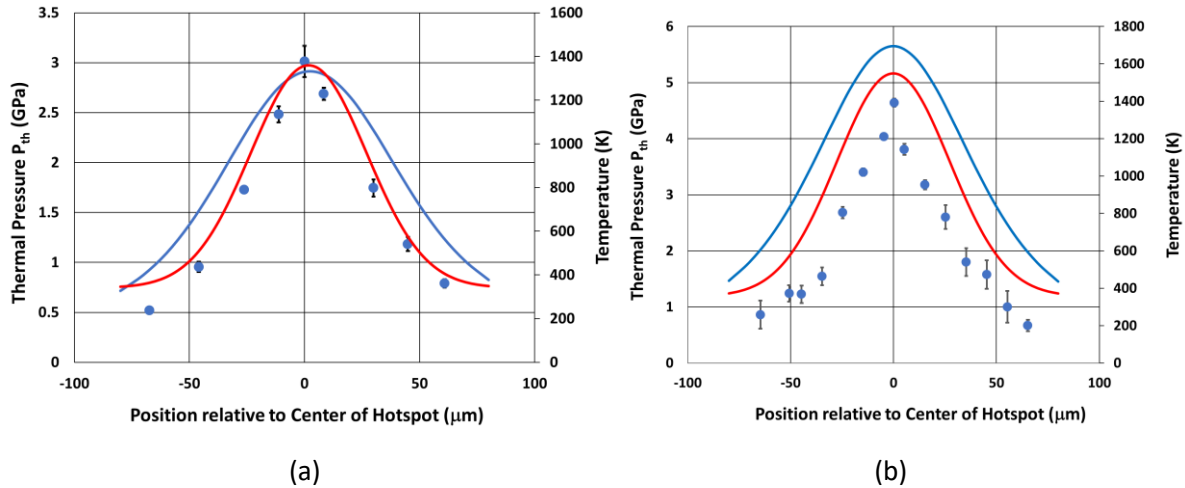
## 98 2 Methods

99 We combine spatially resolved synchrotron X-ray powder diffraction [*Kunz et al.*, 2005; *Laugier and*  
100 *Bochu*, 2002; *Prescher and Prakapenka*, 2015] at distributed points along a BX90 [*Kantor et al.*, 2012]  
101 DAC’s sample chamber’s diameter with a 2-dimensional temperature map [*Kiefer and Duffy*, 2005; *Kunz*  
102 *et al.*, 2018; *Manga and Jeanloz*, 1996; *Rainey and Kavner*, 2014] of the sample chamber through  
103 pressure-volume-temperature (PVT) Murnaghan equation of states (EOS) [*Anderson*, 1997; *Angel et al.*,  
104 2014; *Birch*, 1952; *Helfrich and Connolly*, 2009; *Murnaghan*, 1951] on samples of Agl [*Chauhan and*  
105 *Singh*, 2007; *Hull and Keen*, 1999] and San Carlos olivine [*Liu et al.*, 2005; *Liu and Li*, 2006] to determine  
106 the pressure distribution across the laser heated hotspot. By comparing these pressure values with the  
107 pressures measured at the same positions before the heating event [*H Mao et al.*, 1986], we obtain a  
108 distribution of the thermal pressure ( $P_{\text{th}}$ ) produced by the heating event. More details on the sample  
109 and X-ray diffraction techniques, as well as on the laser heating and temperature mapping are given in  
110 the Supporting Information, Section 1.

111 **3 Results**

112 **3.1 Temperature profiles**

113 Figure 1 shows the temperature profile (red) across the hot spots in Agl and San Carlos olivine. The hot-  
 114 spots can be fit with a Gaussian function (S.I. Table 1), and have approximately the width of the laser  
 115 spot. These are in agreement with the Gaussian intensity distribution of the IR fiber laser, and indicate  
 116 that the coupling of the samples with the laser is not markedly temperature dependent. Both  
 117 temperature curves decrease to basically room temperature at the sample/gasket interface. This  
 118 confirms the highly local nature of the temperature distribution in laser-heated samples within a DAC. It  
 119 is therefore justified to assume that the cold gasket does not suffer any temperature-induced  
 120 deformation: indeed, no irreversible deformation, as manifested by a shift in sample diameter, was  
 121 observed following heating. The heating process of the entire sample volume is thus, to a first  
 122 approximation, isochoric. To second order, it is possible that localized heating of the anvils may produce  
 123 a slight contraction in the axial direction of the sample (even while the radial direction remains  
 124 unchanged): the trade-off between the elastic response of the anvil to the thermal pressure within the  
 125 sample and the thermal pressure induced by localized heating is difficult to characterize, but this effect  
 126 is likely to be small.



127 (a) (b)  
 128  
 129 **Figure 1:** Observed beam temperature across the hotspot (red) and observed (blue symbols) and modeled (blue line) thermal  
 130 pressure in Agl (a) and San Carlos olivine (b). The position of the pressure peak coincides with the hotspot peak as is expected  
 131 for a thermal pressure-induced increase.

132 **3.2 Pressure profiles**

133 Figure 1 also shows the observed thermal pressure distribution (blue dots) across the laser heated  
 134 hotspot (red line) as deduced from the procedure described above and in Supporting Information using  
 135 the thermoelastic constants given in S.I. Table 1.

136 In both samples, a significant pressure peak, that is at the same location as the peak of the hotspot, is  
 137 observed. In Agl, we observe a maximum thermal pressure of ~ 3 GPa at the center of the hotspot  
 138 (~1400 K). It decreases to 0.5 GPa within about 70 μm. At the steepest part of the slope, about 20 μm  
 139 from the center, the pressure drops by about 0.4 GPa per 10 μm. In San Carlos olivine, the situation is  
 140 similar. A pronounced pressure maximum of ~4.5 GPa above the room-temperature value is measured

141 at the center of the hotspot (~1600 K). The thermal gradient is somewhat larger than in AgI, ~1 GPa/10  
142  $\mu\text{m}$ : this difference likely reflects the marked difference in strength between the two materials. It is  
143 notable, however, that even within a weak solid like AgI, the thermal pressure remains localized and  
144 does not fully re-equilibrate through viscous relaxation across the sample over the multi-minute course  
145 of the experiment.

146 Indeed, in both materials the thermal pressure distribution closely traces the temperature distribution,  
147 giving testament to the local nature of thermal pressure as predicted by *Dewaele et al.* [1998] and *Heinz*  
148 [1990]. Nevertheless, an effect that is plausibly associated with material strength can be experimentally  
149 discerned: the peak thermal pressure in AgI is slightly lower and the pressure distribution is wider than  
150 is observed in olivine.

## 151 4 Discussion

152 This is – to the best of our knowledge – the first documented experimental determination of the spatial  
153 distribution of thermal pressure across a laser heated spot within the diamond anvil cell. The general  
154 magnitude of the values reported here correspond quite well to the thermodynamic thermal pressure  
155 ( $\alpha K_0 dT$ ) and also agree well with values predicted by *Heinz* [1990] for his constant volume model. That  
156 model corresponds closely to our experimental arrangement where a sample is loaded without pressure  
157 medium into a DAC and heated locally with a hot spot smaller than the sample volume. As expected, our  
158 values are somewhat higher (when adjusted for the hotspot's peak temperature) than the thermal  
159 pressures predicted by *Dewaele et al.* [1998] using finite element modeling. This is due to the fact that  
160 their modelling set-up included solid or liquid argon surrounding the sample as a pressure transmitting  
161 medium: such rare gas media are expected to be weak at high pressures (and temperatures), although  
162 argon can maintain substantial pressure gradients above ~20 GPa at 300 K [*Klotz et al.*, 2009].

163 The local nature of the observed thermal pressure is due to the finite shear strength of the expanding  
164 sample in a constrained volume. If the heated sample were a liquid or melt with no shear strength, the  
165 thermal pressure would equilibrate over the entire gasket hole. For the material, the size of the heated  
166 spot and sample, and the peak temperatures considered in this study, the equilibrated thermal pressure  
167 would amount to a homogeneous ~1.25 – 1.5 GPa increase across the entire sample volume. The  
168 observed gradients in thermal pressure therefore confirm that the temperatures attained were well  
169 below the melting point: however, even within a material that is expected to be relatively weak (AgI),  
170 thermal pressure-induced pressure increases of several GPa are observed.

171 To simulate the observed localized pressure increases within our samples, our model uses the non-zero  
172 shear strengths of the heated samples as a volumetric shielding mechanism between the colder material  
173 located radially outward from the hot spot, and the thermal expansion of the material within the hot  
174 spot (See Supporting Information Section 2). The volume of the heated material is therefore constrained  
175 to be smaller than the size of the gasket hole. We quantified this simple model by partitioning the  
176 sample volume with radial differential elements centered to the hot-spot. The temperature function was  
177 then derived from a Gaussian approximation of the experimental temperature maps. At a fixed radial  
178 distance, the thermal pressure is determined by assuming a rigid boundary at that fixed radial distance  
179 where the thermal expansion of the nested interior region is allowed to aggregate to a thermal pressure  
180 vector directed radially outwards. The fully rigid boundary construction assumed in our model is akin to

181 an infinite shear strength analogy that completely shields the colder exterior side of the shell from the  
182 hotter interior side. The model thus represents an upper bound on the expected thermal pressure  
183 increase. A detailed description of the model calculations is given in the Supporting Information, Section  
184 2. The predicted pressure distributions of this simple model (blue curve) are compared with the  
185 experimental data (blue dots) in Figure 1. For AgI, the model predicts the peak pressure accurately, but  
186 under-estimates the pressure gradient. In the case of San Carlos olivine, the model predicts a pressure  
187 distribution that is shifted upward from the observed values by about 1 GPa (at an observed peak  
188 pressure of  $\sim 4.5$  GPa). We attribute this discrepancy to the pressure gradient being too steep to be  
189 resolved with a  $10\ \mu\text{m}$  sized X-ray spot thus biasing the measured pressures towards lower values. This  
190 is consistent with the fact that the model matches the measured values much better for AgI where the  
191 lower shear strength allows for a flatter pressure gradient, which is better matched to the  $10\ \mu\text{m}$  X-ray  
192 spot size used. We therefore expect the real pressure increase to be sharper and to lie between the  
193 measured spots and the values given by the model.

194 Our measurements demonstrate that even for soft materials at temperatures close to their melting line,  
195 a significant pressure increase coupled with a pressure gradient around the localized hot spot is  
196 maintained in laser-heated diamond anvil cells. Given the steepness of the observed pressure gradient,  
197 this thermally-induced pressure increase and gradient is also expected to be significant in samples that  
198 are embedded in 'soft' pressure media such as Ne or He where their shear strength at high pressures  
199 becomes sufficient to contain the thermal pressure within the embedded sample (e.g. *Klotz et al.*  
200 [2009]). The shear strengths of the media consequently negate the full pressure-equilibrating effect  
201 expected in hydrostatic media for the pressure generated locally in the sample through local heating.  
202 These findings have ramifications for the design and interpretation of in-situ high-pressure high-  
203 temperature diffraction studies aimed at determining PVT equations of state of Earth materials and  
204 consequently for the mineralogical interpretation of geophysical density profiles based on LHDAC  
205 results.

206 *Ramifications for LHDAC experimental designs:*

- 207 (1) If, during a LHDAC experiment pressure is measured before and after the heating event,  
208 pressure can be significantly underestimated in the center of the hotspot (i.e. where the X-rays usually  
209 probe the sample) during the heating event: such localized, thermally-induced pressurization has not  
210 been previously characterized (e.g. *Andrault et al.* [1998]; *A Kavner and Duffy* [2001] ).
- 211 (2) Pressure measurements using the diffraction lines of a temperature-insulating pressure medium  
212 (i.e. Ne, Ar, He) may similarly underestimate the pressure within the hot sample given the steep  
213 pressure gradients we observed within the hotspot. The underestimation of the pressure derived from  
214 the lattice parameters of a solid, non-laser-absorbing pressure medium (such as NaCl or MgO) could be  
215 larger if the pressure medium simultaneously also acts as a thermal insulation material shielding the  
216 diamonds from the laser hot spot. In that case, it is possible that a significant portion of the diffracting  
217 volume within the pressure medium is also at a temperature significantly below the peak temperature.
- 218 (3) As a consequence of (1) and (2), the most reliable pressure determination in a laser heated  
219 diamond anvil cell is likely generated by a pressure standard that is intimately mixed with the sample,  
220 monitored in situ at simultaneous high temperature and pressure, and which differs from the material  
221 used to thermally insulate the diamonds from the sample. Ideally, such an internal calibrant (often Pt)  
222 would also be chemically inert at extreme conditions in order to avoid unwanted chemical reaction or  
223 alloying with the sample. Such a mixed phase geometry can be particularly effective when deployed in

224 instances where the calibrant itself is used as the laser-absorber within the sample (e.g. *Tateno et al.*  
225 [2019]).

226 (4) The observed steep gradients in thermal pressure demonstrate that a straightforward means of  
227 experimental optimization, in terms of sampling a spot at well-constrained pressure and temperature, is  
228 to combine a large uniform hot spot (which can be generated using beam shaping optics, such as a Pi  
229 shaper) with the smallest possible X-ray probe. Naturally, a small X-ray beam has the inherent problem  
230 of reduced data quality due to a decrease in powder statistics. This is especially true at high  
231 temperatures where recrystallization and grain growth are often observed (e.g. [*Irifune et al.*, 2005] ,  
232 [*Shen et al.*, 1998]). While poor powder diffraction statistics might still allow extraction of reliable  
233 volumetric data, other approaches could involve dispensing with monochromatic powder diffraction for  
234 PVT equation of state determinations based on diffraction. Single crystal and multigrain diffraction  
235 techniques are obvious alternatives that are commonly deployed at ambient temperatures, but are  
236 difficult (although not in principle impossible) to combine with laser heating, due to the requirement  
237 that the sample be rotated relative to the X-ray beam [*Dubrovinsky et al.*, 2010]. X-ray Laue  
238 microdiffraction can be a useful tool in cases where a sample cannot easily be rotated as required on a  
239 monochromatic single crystal diffractometer (e.g. *Barkov et al.* [2019]; *Tamura et al.* [2002]). However,  
240 in the absence of energy resolving area detectors, the application of Laue microdiffraction to PVT  
241 equation of state studies is not practical. A potentially viable technique that can be deployed using  
242 commonly available equipment is energy resolved Laue diffraction, which can use a scanning  
243 monochromator rather than an energy resolving detector. To make this approach feasible in the  
244 traditional transmission geometry employed in laser heating set-ups (e.g. *Kunz et al.* [2018], *Shen et al.*  
245 [2001]) requires a large energy range ( $\sim 15 \text{ keV} < E < 50 \text{ keV}$ ) to be covered in order to overcome the low  
246 density in reciprocal space coverage at low diffraction angles (e.g. *Kunz et al.* [2009]). Alternatively, a  
247 set-up where the laser heating is in the axial direction through the diamonds, but the detector is  
248 positioned at 90 degrees (i.e. signal through X-ray transparent gasket) could be envisaged.

249  
250 The key point here is that the sharply peaked pressure distributions that we document within laser-  
251 heated spots motivate either smaller X-ray probes (and larger heated spots) than have previously been  
252 deployed, or alternate diffraction techniques to enhance the spatial resolution of the X-ray probe itself.

253 *Ramifications for geophysical models derived based on LHDA experiments:*

254 A systematic off-set in the assumed pressures for PVT equation of states, as would occur if part of the  
255 induced thermal pressure is not recognized, has consequences for the geophysical conclusions deduced  
256 from such experiments. As an example, we tested the effect on a hypothetical experiment on  
257 bridgmanite ( $\text{Mg}_{(1-x)}\text{Fe}_x\text{SiO}_3$  ( $x = 0.12$ )). We created a synthetic PVT dataset with pre-heated pressures  
258 between  $\sim 25$  and 100 GPa and 3 different mantle relevant temperatures (2000, 2500 and 3000 K), with  
259 imposed thermoelastic parameters ( $V_0$ ,  $K_0$ ,  $K'$ , Anderson-Grüneisen  $\delta$ ,  $\alpha_0$ ,  $d\alpha/dP$ ) derived from the  
260 literature and tabulated in Table 1. We add to the pre-heated pressure a thermal pressure of  $\alpha K \Delta T$  (8.4,  
261 10.9, 13.3 GPa), assuming an  $\alpha K \sim 5 \times 10^{-3} \text{ GPa/K}$  in accordance with our measurements. We then use  
262 these synthetic  $V/V_0 - T$  data to fit a Murnaghan equation of state by assuming pressures that  
263 underestimated the total pressure by 2 GPa. This process yields a set of thermoelastic properties that  
264 are biased through the neglect of this thermal pressure (Table 1). As can be seen from Table 1, both the  
265 Anderson-Grüneisen parameter  $\delta$  ( $dK/dT$ ) and  $d\alpha/dP$  refine towards values that predict a density vs  
266 pressure curve that is shifted positively (to higher densities) relative to the true values (Figure 2). If such

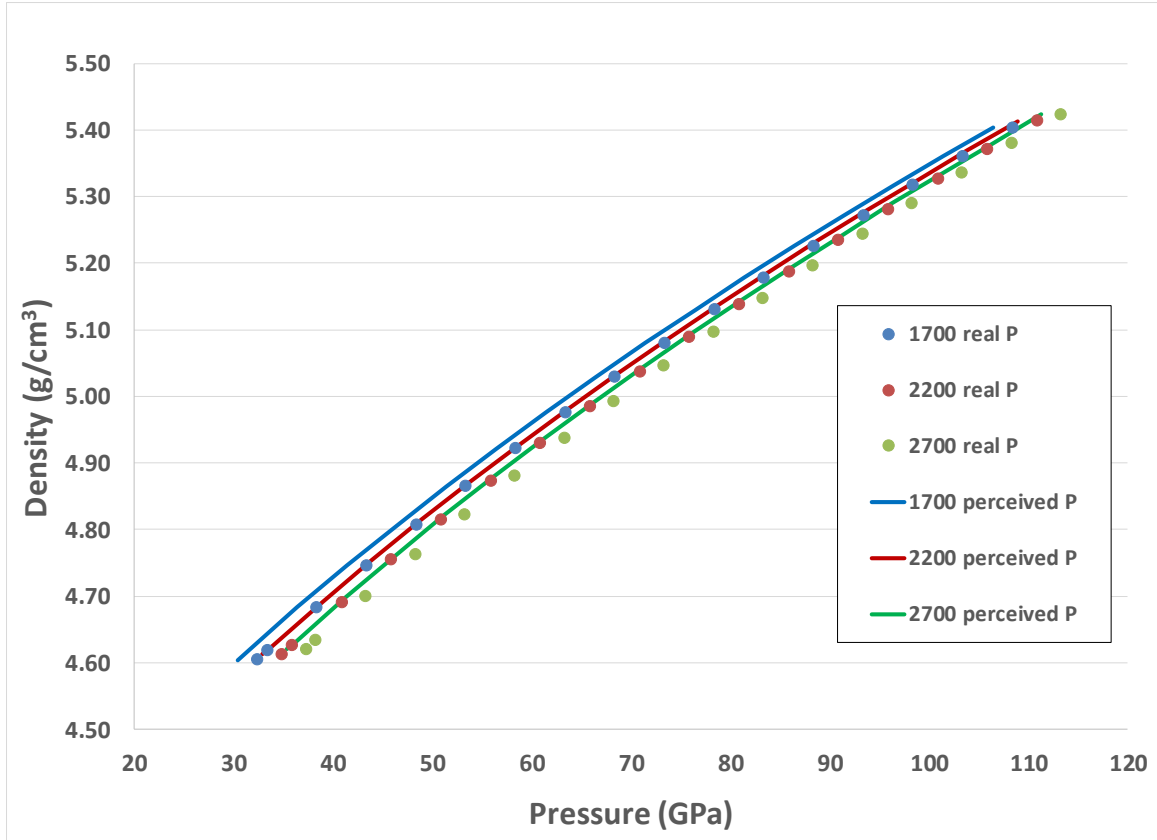
267 a slightly overestimated density vs depth (i.e. P and T) profile were compared with seismic data to  
 268 estimate the Fe content in bridgmanite in the Earth's mantle, this density difference would lead to an  
 269 underestimate of the Fe content in the mantle. For our model parameters, the sensitivity of the system  
 270 is such that even this small neglect of thermal pressure would generate an underestimate of the deep  
 271 mantle's inferred Fe number (based on a too-dense EOS) of  $\sim 0.03$ .

	"Synthetic" values	Refined values
$V_0$	163.7 <sup>1)</sup>	Not refined
$K_0$	246.7 <sup>1)</sup>	230.2(5)
$K'$	4.03 <sup>1)</sup>	4.40(1)
Anderson-Grüneisen $\delta$	3.25 <sup>2)</sup>	1.74(6)
$\alpha_0$	$2.0 \times 10^{-5}$ <sup>3)</sup>	$1.63(2) \times 10^{-5}$
$d\alpha/dP$	$-1.0 \times 10^{-7}$ <sup>3)</sup>	$-1.01(2) \times 10^{-7}$

272

273 **Table 1: Thermoelastic parameters for the "synthetic" Bridgmanite that were used to create ideal  $V/V_0(P,T)$  values together**  
 274 **with the corresponding values obtained from fitting a Murnaghan equation against the same  $V/V_0$  and T but P points**  
 275 **underestimated by 2 GPa. See text for more details. 1) *Shukla et al.* [2016]; 2) The 'synthetic'  $\delta$  is estimated by equating  $K(0)$**   
 276 **+  $dK/dT \times \Delta T = K_0 \times [1 + \alpha(P) \times \Delta(T)]^{-6}$  and solving for  $\delta$ . A  $dK/dT$  of  $\sim -0.01$  is assumed for this [*Shukla et al.*, 2016]],  $\alpha(P)$  is**  
 277 **assumed to be  $\sim 1.6 \times 10^{-7}$  for this (*Wang et al.* [1994]. 3) *Utsumi et al.* [1995]**

278



279

280 **Figure 2: Density versus pressure values for synthetic ideal  $(\text{Mg}_{0.88}\text{Fe}_{0.12})\text{SiO}_3$  bridgmanite at three different temperatures**  
 281 **with thermal pressure contributions corresponding to  $\alpha K_T dT$ ; and curves derived from thermoelastic properties as obtained**  
 282 **from a PVT data set that underestimates the thermal pressure by 2 GPa (“perceived P”). This difference can for example lead**  
 283 **to a wrong estimation of the Fe content of the phase considered (see text).**

284 We note also that the local character of the thermal pressure elevations that we observe (Figure 1)  
 285 suggests possible experimental avenues to measure difficult-to-characterize thermodynamic derivative  
 286 properties. In particular, the sample translation techniques that we have documented can be deployed  
 287 to measure the thermal pressure distributions within specially designed sample configurations. In  
 288 particular, as shown in the Supporting Information Section 3, for a sample suspended in a medium that  
 289 is of extremely high rigidity (e.g. diamond), the change in thermal pressure should reflect the  
 290 thermodynamic value of  $\alpha K_T dT$ . As such, if the thermal pressure can be assessed at two (or more)  
 291 different pressures at high temperatures, the thermodynamic relation of  $\alpha K_T$  (at  $P, T$ ) -  $\alpha K_T$  (at  $P_0, T$ )  
 292 being equal to the volumetric integral of  $(\delta_T - K'_T)d\ln V$  can be deployed to provide a direct measure  
 293 (assuming  $K'$  is constrained from equation of state measurements) of the Anderson-Grüneisen  
 294 parameter at extreme conditions (e.g. *Anderson and Isaak [1993]; Jackson and Rigden [1996]*). The  
 295 Anderson-Grüneisen parameter, which dictates the volume dependence of thermal expansion, is  
 296 difficult to constrain at high pressures: it is inferred to decrease with compression, but its pressure  
 297 dependence is not well known (*Anderson and Isaak [1993]*). In passing, we note that the other end-  
 298 member, measurement of thermal pressure within a medium with zero strength (and high gasket  
 299 strength), could also be deployed to constrain the pressure dependence of thermal pressure. In this  
 300 instance, an accurate characterization of both the volume of the heated sample and of the sample  
 301 chamber as a whole would be required to accurately interpret the sample-wide thermal pressure

302 increase. Hence, our present measurements demonstrate that, with appropriate experimental designs,  
303 accurate constraints on the pressure-dependence of the Anderson-Grüneisen parameter could be  
304 generated.

## 305 5 Conclusion:

306 We present the first quantitative experimental characterization of the pressure gradients caused  
307 by thermal pressures induced by temperature gradients in the laser-heated diamond anvil cell. The  
308 observed pressure increases correspond in magnitude to previously published theoretical and modeled  
309 values, and are also in accord with the thermodynamically expected value: the dominant parameter that  
310 governs the magnitude of thermal pressure is, unsurprisingly, the product of thermal expansion and the  
311 bulk modulus. Our results indicate that there is a nuanced effect on thermal pressure associated with  
312 material strength, thus showing that some diffusion of the stress field occurs within the samples. In  
313 particular, our results on AgI are both lower in their peak thermal pressure and have smaller spatial  
314 gradients of pressure with distance, which is consistent with AgI being weaker than olivine. Our simple  
315 modeling overestimates the thermal pressures accessed by olivine. We attribute this to the fact that the  
316 model provides an upper limit on the thermal pressure, combined with the fact that our X-ray probe is  
317 relatively large (10  $\mu\text{m}$ ) compared to the steepness of the pressure gradient (this is especially acute in  
318 olivine, where the observed pressure gradients are  $\sim 1 \text{ GPa}/10 \mu\text{m}$ ).

319 From an overarching perspective, our results clearly demonstrate that thermal pressures within  
320 laser-heated spots can be substantial and, even within relatively weak materials (AgI), remain localized  
321 around the laser-heated hot spot. As such, high-pressure/high-temperature measurements of  
322 (particularly) derivative parameters, such as thermal expansion at high pressures, likely require either  
323 multiple internal standards and/or a liquid medium to ensure that thermal expansions at extreme  
324 conditions are not underestimated. We also show that only a partial neglect of the thermal pressure can  
325 result in errors of the derived thermos-elastic properties that lead towards higher density at given P and  
326 T conditions. This in turns will cause significant errors on the correlation between density and  
327 mineralogy. Finally, our experimental design for measuring the spatial variations of thermal pressure  
328 could be deployed to quantitatively measure the pressure dependence of thermal pressure, and hence  
329 provide a direct constraint on the variation in the Anderson-Grüneisen parameter at deep planetary  
330 conditions.

## 331 Acknowledgments:

332 All raw data and analysis (diffraction images, temperature maps, pressure calculations, and density vs  
333 pressure analysis) are deposited in Dryad data repository (<https://doi.org/10.7941/D1F63W>).

334 X-ray diffraction experiments were performed at the Advanced Light Source (ALS) beamline 12.2.2. The  
335 ALS is supported by the Director, Office of Science, Office of Basic Energy Sciences, Materials Sciences  
336 Division, of the US Department of Energy under Contract No. DE-AC03-76SF00098 at the Lawrence  
337 Berkeley National Laboratory and the University of California, Berkeley. Sample preparation benefitted  
338 from the ALS laser mill purchased by the Consortium for Materials Properties Research in Earth Sciences;

339 COMPRES supported this project under the NSF Cooperative Agreement EAR 16-49658. QW is supported  
340 by NSF EAR-1620423. EY was supported by a private fund (Yen-Zantua).

341 Discussions with Dion Heinz greatly improved this manuscript and are warmly acknowledged. A special  
342 thanks is owed to Howard Padmore who not only helped fund this project, but also acted as a mentor  
343 and source of inspiration.

344 **References**

- 345 Anderson, O. L. (1997), The volume dependence of thermal pressure in solids, *Journal of Physics and*  
346 *Chemistry of solids*, 58(2), 335-343.
- 347 Anderson, O. L., and D. G. Isaak (1993), The dependence of the Anderson-Grüneisen parameter  $\delta T$  upon  
348 compression at extreme conditions, *Journal of Physics and Chemistry of Solids*, 54(2), 221-227.
- 349 Andraut, D., G. Fiquet, J.-P. Itie, P. Richet, P. Gillet, D. Hausermann, and M. Hanfland (1998), Thermal  
350 pressure in the laser-heated diamond-anvil cell; an X-ray diffraction study, *European Journal of*  
351 *Mineralogy*, 10(5), 931-940.
- 352 Angel, R. J., M. Alvaro, and J. Gonzalez-Platas (2014), EosFit7c and a Fortran module (library) for  
353 equation of state calculations, *Zeitschrift für Kristallographie-Crystalline Materials*, 229(5), 405-419.
- 354 Barkov, A. Y., L. Bindi, N. Tamura, G. I. Shvedov, B. Winkler, C. V. Stan, W. Morgenroth, R. F. Martin, F.  
355 Zaccarini, and C. J. Stanley (2019), Ognitite, NiBiTe, a new mineral species, and Co-rich maucherite from  
356 the Ognit ultramafic complex, Eastern Sayans, Russia, *Mineralogical Magazine*, 83(5), 695-703.
- 357 Bassett, W. A. (2016), Diamond Anvil Cells: Laser Heating of Samples at High Pressure: 50 Years, *Laser*  
358 *Focus World*.
- 359 Birch, F. (1952), Elasticity and constitution of the Earth's interior, *Journal of Geophysical Research*, 57(2),  
360 227-286.
- 361 Chauhan, R., and C. Singh (2007), Equation of state and thermal expansivity of NaCl under high pressure  
362 and high temperature, *Physica B: Condensed Matter*, 387(1-2), 352-357.
- 363 Dewaele, A., G. Fiquet, and P. Gillet (1998), Temperature and pressure distribution in the laser-heated  
364 diamond-anvil cell, *Review of scientific instruments*, 69(6), 2421-2426.
- 365 Dorogokupets, P., A. Dymshits, T. Sokolova, B. Danilov, and K. Litasov (2015), The equations of state of  
366 forsterite, wadsleyite, ringwoodite, akimotoite, MgSiO<sub>3</sub>-perovskite, and postperovskite and phase  
367 diagram for the Mg<sub>2</sub>SiO<sub>4</sub> system at pressures of up to 130 GPa, *Russian Geology and Geophysics*, 56(1-  
368 2), 172-189.
- 369 Dubrovinsky, L., T. Boffa-Ballaran, K. Glazyrin, A. Kurnosov, D. Frost, M. Merlini, M. Hanfland, V.  
370 Prakapenka, P. Schouwink, and T. Pippinger (2010), Single-crystal X-ray diffraction at megabar pressures  
371 and temperatures of thousands of degrees, *High Pressure Research*, 30(4), 620-633.
- 372 Fiquet, G., D. Andraut, A. Dewaele, T. Charpin, M. Kunz, and D. Hausermann (1998), PVT equation of  
373 state of MgSiO<sub>3</sub> perovskite, *Physics of the Earth and Planetary Interiors*, 105(1-2), 21-31.
- 374 Fiquet, G., D. Andraut, J. Itie, P. Gillet, and P. Richet (1996), X-ray diffraction of periclase in a laser-  
375 heated diamond-anvil cell, *Physics of the Earth and Planetary Interiors*, 95(1-2), 1-17.
- 376 Heinz, D. L. (1990), Thermal pressure in the laser-heated diamond anvil cell, *Geophysical Research*  
377 *Letters*, 17(8), 1161-1164.
- 378 Helffrich, G., and J. Connolly (2009), Physical contradictions and remedies using simple polythermal  
379 equations of state, *American Mineralogist*, 94(11-12), 1616-1619.
- 380 Hull, S., and D. Keen (1999), Pressure-induced phase transitions in AgCl, AgBr, and AgI, *Physical Review*  
381 *B*, 59(2), 750.
- 382 Irifune, T., M. Isshiki, and S. Sakamoto (2005), Transmission electron microscope observation of the  
383 high-pressure form of magnesite retrieved from laser heated diamond anvil cell, *Earth and Planetary*  
384 *Science Letters*, 239(1-2), 98-105.
- 385 Ismailova, L., E. Bykova, M. Bykov, V. Cerantola, C. McCammon, T. B. Ballaran, A. Bobrov, R. Sinmyo, N.  
386 Dubrovinskaia, and K. Glazyrin (2016), Stability of Fe, Al-bearing bridgmanite in the lower mantle and  
387 synthesis of pure Fe-bridgmanite, *Science advances*, 2(7), e1600427.
- 388 Jackson, I., and S. M. Rigden (1996), Analysis of PVT data: constraints on the thermoelastic properties of  
389 high-pressure minerals, *Physics of the earth and planetary interiors*, 96(2-3), 85-112.

390 Kantor, I., V. Prakapenka, A. Kantor, P. Dera, A. Kurnosov, S. Sinogeikin, N. Dubrovinskaia, and L.  
 391 Dubrovinsky (2012), BX90: A new diamond anvil cell design for X-ray diffraction and optical  
 392 measurements, *Review of Scientific Instruments*, *83*(12), 125102.

393 Kavner, A., and T. S. Duffy (2001), Strength and elasticity of ringwoodite at upper mantle pressures,  
 394 *Geophysical Research Letters*, *28*(14), 2691-2694.

395 Kavner, A., and C. Nugent (2008), Precise measurements of radial temperature gradients in the laser-  
 396 heated diamond anvil cell, *Review of Scientific Instruments*, *79*(2), 024902.

397 Kiefer, B., and T. S. Duffy (2005), Finite element simulations of the laser-heated diamond-anvil cell,  
 398 *Journal of Applied Physics*, *97*(11), 114902.

399 Klotz, S., J. Chervin, P. Munsch, and G. Le Marchand (2009), Hydrostatic limits of 11 pressure  
 400 transmitting media, *Journal of Physics D: Applied Physics*, *42*(7), 075413.

401 Komabayashi, T., and Y. Fei (2010), Internally consistent thermodynamic database for iron to the Earth's  
 402 core conditions, *Journal of Geophysical Research: Solid Earth*, *115*(B3).

403 Kunz, M., A. A. MacDowell, W. A. Caldwell, D. Cambie, R. S. Celestre, E. E. Domning, R. M. Duarte, A. E.  
 404 Gleason, J. M. Glossinger, and N. Kelez (2005), A beamline for high-pressure studies at the Advanced  
 405 Light Source with a superconducting bending magnet as the source, *Journal of synchrotron radiation*,  
 406 *12*(5), 650-658.

407 Kunz, M., N. Tamura, K. Chen, A. A. MacDowell, R. S. Celestre, M. M. Church, S. Fakra, E. E. Domning, J.  
 408 M. Glossinger, and J. L. Kirschman (2009), A dedicated superbend X-ray microdiffraction beamline for  
 409 materials, geo-, and environmental sciences at the advanced light source, *Review of Scientific  
 410 Instruments*, *80*(3), 035108.

411 Kunz, M., J. Yan, E. Cornell, E. E. Domning, C. E. Yen, A. Doran, C. M. Beavers, A. Treger, Q. Williams, and  
 412 A. A. MacDowell (2018), Implementation and application of the peak scaling method for temperature  
 413 measurement in the laser heated diamond anvil cell, *Review of Scientific Instruments*, *89*(8), 083903.

414 Laugier, J., and B. Bochu (2002), CELREF V3: Cell parameters refinement program from powder  
 415 diffraction diagram. Laboratoire des Matériaux et du Génie Physique, Institut National Polytechnique de  
 416 Grenoble, France, edited.

417 Liu, W., J. Kung, and B. Li (2005), Elasticity of San Carlos olivine to 8 GPa and 1073 K, *Geophysical  
 418 Research Letters*, *32*(16).

419 Liu, W., and B. Li (2006), Thermal equation of state of (Mg<sub>0.9</sub>Fe<sub>0.1</sub>)<sub>2</sub>SiO<sub>4</sub> olivine, *Physics of the Earth  
 420 and Planetary Interiors*, *157*(3-4), 188-195.

421 Manga, M., and R. Jeanloz (1996), Axial temperature gradients in dielectric samples in the laser-heated  
 422 diamond cell, *Geophysical research letters*, *23*(14), 1845-1848.

423 Mao, H., J.-A. Xu, and P. Bell (1986), Calibration of the ruby pressure gauge to 800 kbar under quasi-  
 424 hydrostatic conditions, *Journal of Geophysical Research: Solid Earth*, *91*(B5), 4673-4676.

425 Mao, W., G. Shen, V. B. Prakapenka, Y. Meng, A. J. Campbell, D. L. Heinz, J. Shu, R. J. Hemley, and H.-K.  
 426 Mao (2004), Ferromagnesian postperovskite silicates in the D "layer of the Earth, *Proceedings of the  
 427 National Academy of Sciences of the United States of America*, *101*(45), 15867-15869.

428 Marquardt, H., and K. Marquardt (2012), Focused ion beam preparation and characterization of single-  
 429 crystal samples for high-pressure experiments in the diamond-anvil cell, *American Mineralogist*, *97*(2-3),  
 430 299-304.

431 Meng, Y., D. J. Weidner, and Y. Fei (1993), Deviatoric stress in a quasi-hydrostatic diamond anvil cell:  
 432 Effect on the volume-based pressure calibration, *Geophysical Research Letters*, *20*(12), 1147-1150.

433 Mezouar, M., R. Giampaoli, G. Garbarino, I. Kantor, A. Dewaele, G. Weck, S. Boccato, V. Svitlyk, A. Rosa,  
 434 and R. Torchio (2017), Methodology for in situ synchrotron X-ray studies in the laser-heated diamond  
 435 anvil cell, *High Pressure Research*, *37*(2), 170-180.

436 Morard, G., D. Andrault, D. Antonangeli, Y. Nakajima, A. Auzende, E. Boulard, S. Cervera, A. Clark, O.  
 437 Lord, and J. Siebert (2017), Fe–FeO and Fe–Fe<sub>3</sub>C melting relations at Earth's core–mantle boundary

438 conditions: Implications for a volatile-rich or oxygen-rich core, *Earth and Planetary Science Letters*, 473,  
439 94-103.

440 Murnaghan, F. D. (1951), *Finite deformation of an elastic solid*, John Wiley & Sons.

441 Panero, W., and R. Jeanloz (2001), Temperature gradients in the laser-heated diamond anvil cell, *Journal*  
442 *of Geophysical Research: Solid Earth*, 106(B4), 6493-6498.

443 Prescher, C., and V. B. Prakapenka (2015), DIOPTAS: a program for reduction of two-dimensional X-ray  
444 diffraction data and data exploration, *High Pressure Research*, 35(3), 223-230.

445 Rainey, E., and A. Kavner (2014), Peak scaling method to measure temperatures in the laser-heated  
446 diamond anvil cell and application to the thermal conductivity of MgO, *Journal of Geophysical Research:*  
447 *Solid Earth*, 119(11), 8154-8170.

448 Shen, G., and H. K. Mao (2016), High-pressure studies with x-rays using diamond anvil cells, *Reports on*  
449 *Progress in Physics*, 80(1), 016101.

450 Shen, G., H. k. Mao, R. J. Hemley, T. S. Duffy, and M. L. Rivers (1998), Melting and crystal structure of  
451 iron at high pressures and temperatures, *Geophysical Research Letters*, 25(3), 373-376.

452 Shen, G., M. L. Rivers, Y. Wang, and S. R. Sutton (2001), Laser heated diamond cell system at the  
453 Advanced Photon Source for in situ X-ray measurements at high pressure and temperature, *Review of*  
454 *Scientific Instruments*, 72(2), 1273-1282.

455 Shukla, G., M. Cococcioni, and R. M. Wentzcovitch (2016), Thermoelasticity of Fe<sup>3+</sup>-and Al-bearing  
456 bridgmanite: Effects of iron spin crossover, *Geophysical Research Letters*, 43(11), 5661-5670.

457 Tamura, N., R. Celestre, A. MacDowell, H. Padmore, R. Spolenak, B. Valek, N. Meier Chang, A. Manceau,  
458 and J. Patel (2002), Submicron x-ray diffraction and its applications to problems in materials and  
459 environmental science, *Review of scientific instruments*, 73(3), 1369-1372.

460 Tateno, S., T. Komabayashi, K. Hirose, N. Hirao, and Y. Ohishi (2019), Static compression of B2 KCl to 230  
461 GPa and its PVT equation of state, *American Mineralogist*, 104(5), 718-723.

462 Utsumi, W., N. Funamori, T. Yagi, E. Ito, T. Kikegawa, and O. Shimomura (1995), Thermal expansivity of  
463 MgSiO<sub>3</sub> perovskite under high pressures up to 20 GPa, *Geophysical Research Letters*, 22(9), 1005-1008.

464 Wang, Y., D. J. Weidner, R. C. Liebermann, and Y. Zhao (1994), PVT equation of state of (Mg, Fe) SiO<sub>3</sub>  
465 perovskite: constraints on composition of the lower mantle, *Physics of the Earth and Planetary Interiors*,  
466 83(1), 13-40.

467 Williams, Q., E. Knittle, and R. Jeanloz (1991), The high-pressure melting curve of iron: A technical  
468 discussion, *Journal of Geophysical Research: Solid Earth*, 96(B2), 2171-2184.

469

Figure 1a.

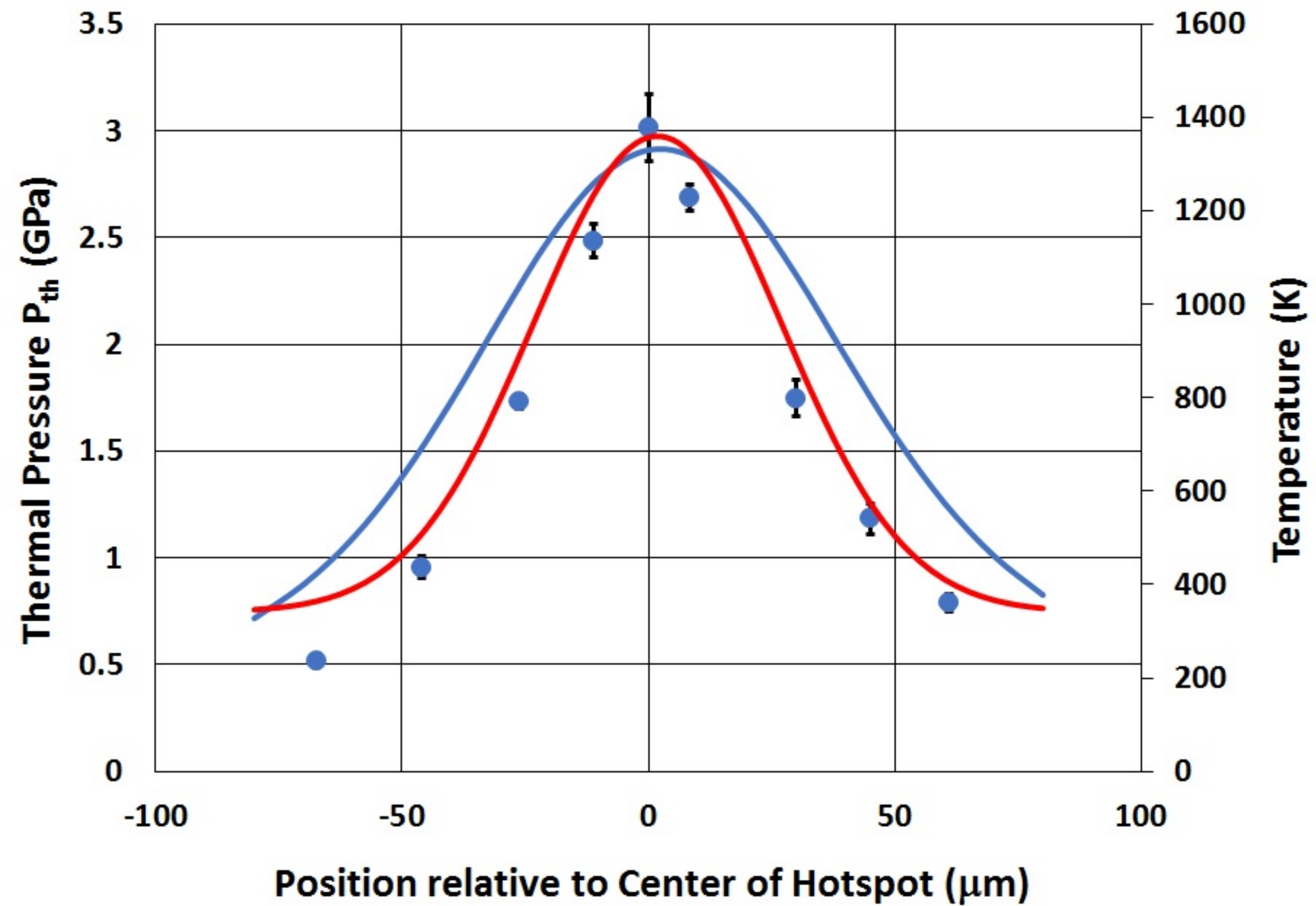


**Figure 1b.**

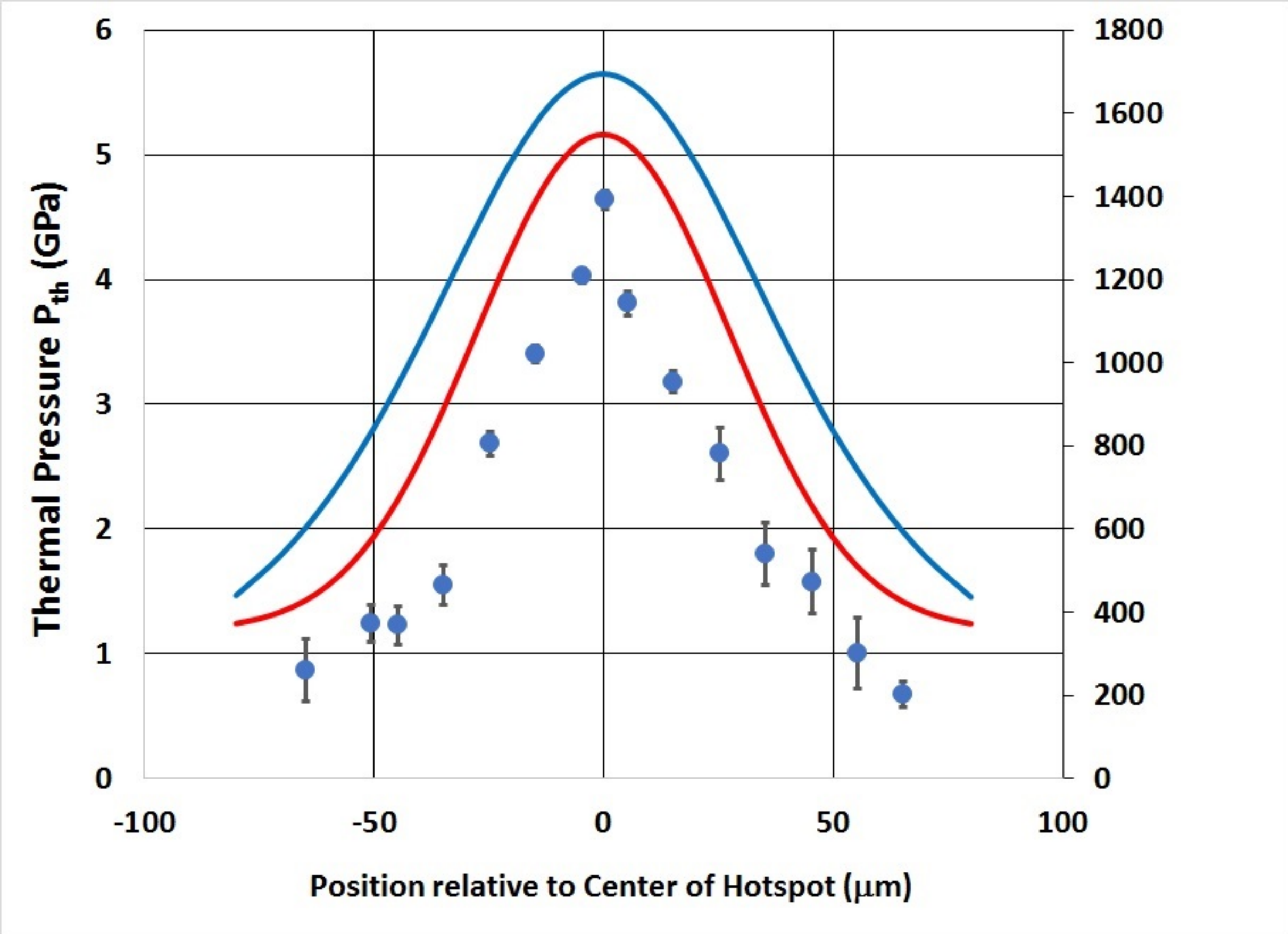
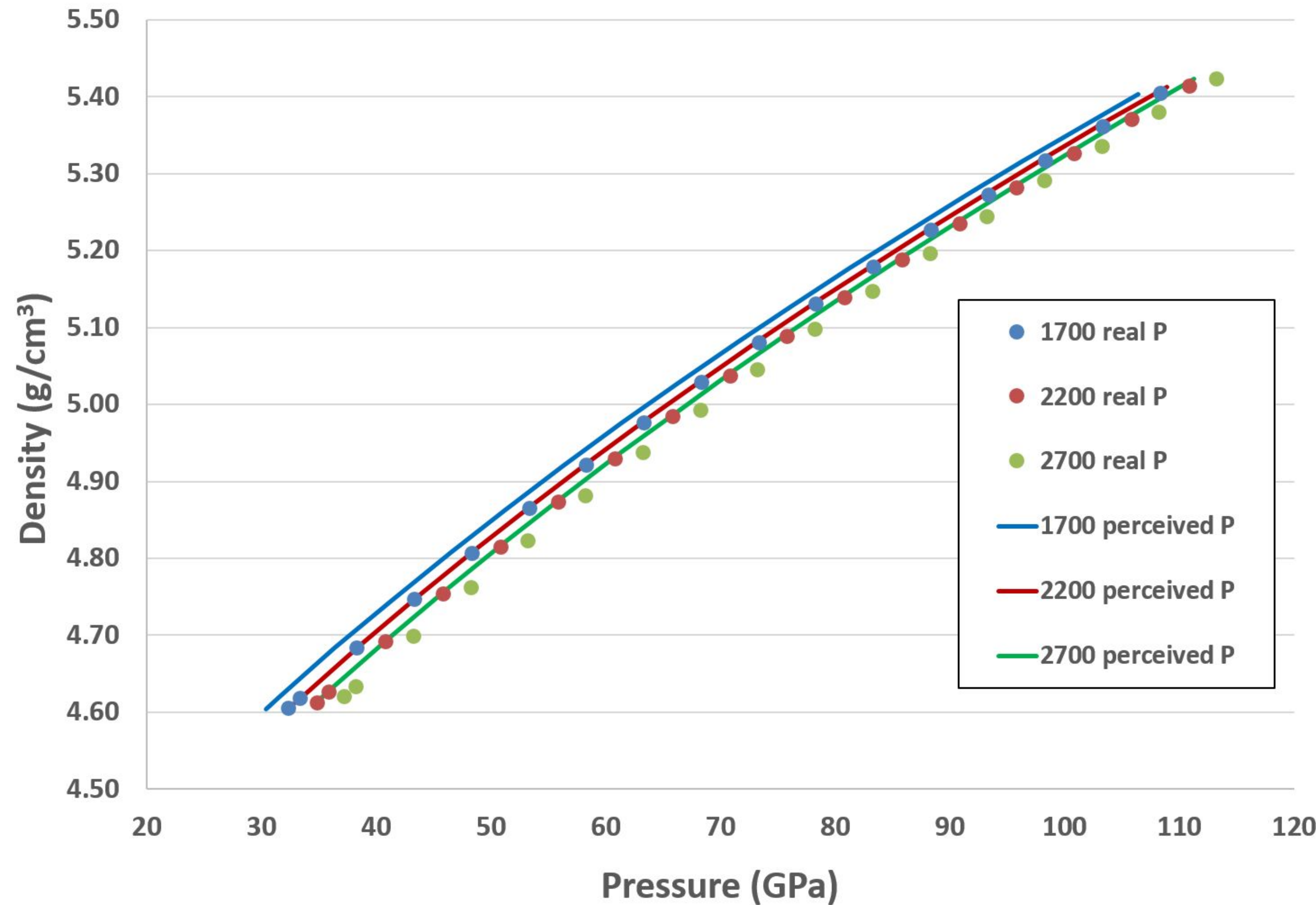


Figure 2.





*Geophysical Research Letters*

Supporting Information for

**Thermal Pressure in the Laser Heated Diamond Anvil Cell: A Quantitative Study and Implications for the Density vs. Mineralogy Correlation of the Mantle**

Connor Ethan Yen, Quentin Williams, and Martin Kunz

## Contents of this File

Here we cover the exact experimental design, including the sample and Laser Heated Diamond Anvil Cell preparation, the specifics of the diffraction setup, and the computational methods of determining beam temperature. We also include here the mathematical derivation of our model.

## Introduction

Section 1 covers the experimental design and Section 2 covers the derivation of our model; Section 3 derives the thermodynamic thermal pressure.

# 1 Experimental Design

## 1.1 Sample preparation

Experiments were performed on commercially available silver iodide, AgI (SIGMA-ALDRICH), and gem-quality San Carlos olivine,  $(\text{Mg}_{0.9}, \text{Fe}_{0.1}^{2+})_2\text{SiO}_4$ . See S.I. Table 1 for thermoelastic parameters. Our choice of these two compounds is motivated both by each material having notably uniform and stable coupling with infrared laser heating, but also by the product of thermal expansion and bulk modulus ( $\alpha K_0$ ) of the two materials being almost equivalent (S.I. Table 1), while their strengths are expected to markedly differ. Accordingly, these two materials provide a means for experimentally demonstrating whether shear strength exercises a major role on thermal pressure, or whether thermal pressure is largely governed by the thermodynamics of local heating of a nearly isochoric system.

	AgI	San Carlos Olivine
Bulk Modulus ( $K_0$ )	42(2) GPa (1)	129.4(4) GPa (2)
$dK/dP$ ( $K'$ )	3.8(3) (1)	4.6(1) (2)
Thermal Expansion ( $\alpha$ )	$8 \times 10^{-5}/\text{K}$ (3)	$2.7(3) \times 10^{-5}/\text{K}$ (4)
Anderson-Grüneisen Parameter ( $\delta$ )	3.8(3)	4.6(1)
$\alpha K_0$	$3.36 \times 10^{-3}$ GPa/K	$3.49 \times 10^{-3}$ GPa/K

**S.I. Table 1:** Thermoelastic parameters of AgI and San Carlos olivine at ambient pressure and temperature. (1) *Hull and Keen* [1999](2) *Liu et al.* [2005], (3) The value for NaCl was used as an approximation *Chauhan and Singh* [2007], (4) *Liu and Li* [2006]. The Anderson-Grüneisen Parameter was set equal to  $dK/dP$ : this assumes that the isothermal derivative with respect to volume of  $\alpha K_T$  is negligible, and represents a good approximation for both halides and olivine [*Anderson*, 1997].

The samples were powdered using a mortar and pestle, and x-ray powder diffraction of the samples at modest pressures (2 – 4 GPa) and room temperature confirmed their chemical purity. High pressures were generated using a BX90 diamond anvil cell [*Kantor et al.*, 2012], with type 2a CVD diamonds (400 $\mu\text{m}$  culets). Steel was used as the gasket material, which was pre-indented to a thickness of 100 $\mu\text{m}$ , and laser drilled to yield sample chambers of 160 $\mu\text{m}$  in diameter. Before loading, parallel tungsten blocks were used to compact the powdered samples. To further reduce sample porosity, the gasket was loaded with the compacted sample, modestly pressurized (< 3 GPa), and then loaded with more sample. Initial cold pressures were determined to be 3-4 GPa for the AgI, and 2-3 GPa for the San Carlos olivine using R-line fluorescence on a cluster of ruby chips placed close to the center of the sample chamber [*Mao et al.*, 1986]. The samples were loaded without a pressure medium or thermal insulation material in order to keep artifacts due to insufficient geometric control of a multi-component sample assembly at a minimum. The lack of inclusion of a thermal insulation layer is justified in samples (like AgI and olivine) where the low thermal conductivity allows the sample in the center of the chamber to be robustly heated by the IR laser without draining its temperature through the diamond heat sinks. In essence, the sample layer in contact with the diamonds acts as the insulation layer for the bulk sample, and the sample itself therefore serves as its own thermal insulation layer. As shown by *Manga*

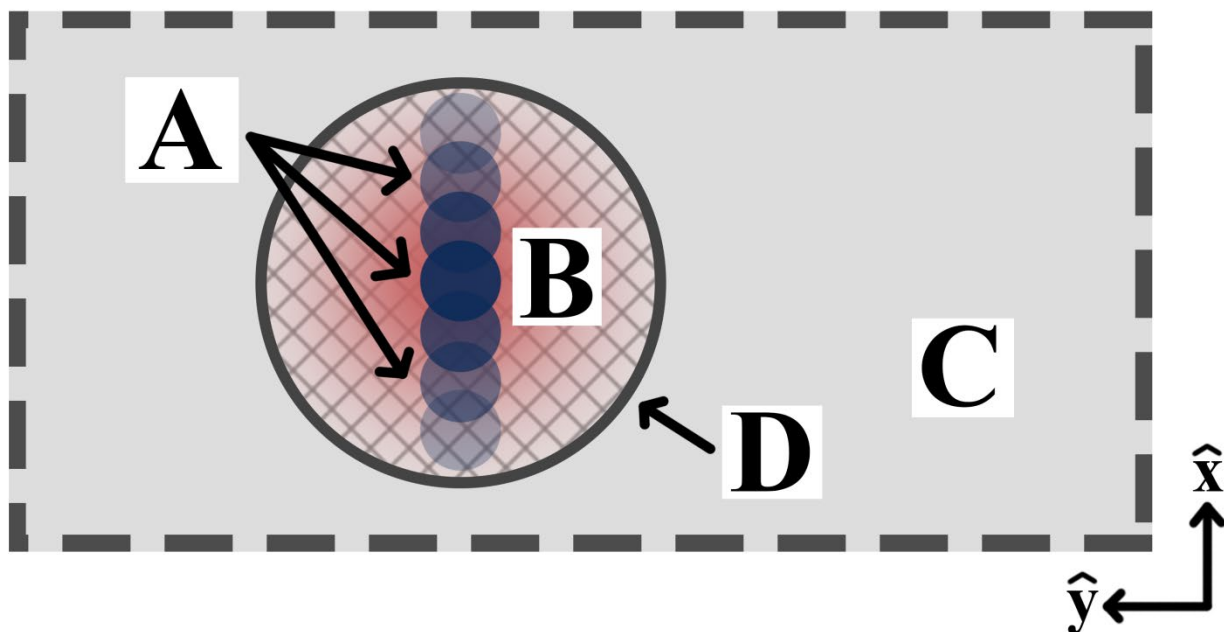
and Jeanloz [1996], the axial temperature gradients expected in a dielectric material have a negligible effect on the temperature deduced from the observed thermal radiation spectrum. Furthermore, the lack of any observable peak broadening or splitting within the hot powder diffraction patterns indicates that the axial thermal gradients are very steep, and therefore the cold insulation layer is too thin to affect the diffraction patterns and thus bias the deduced thermal pressures.

## 1.2 Synchrotron X-ray diffraction

Angle-dispersive in situ X-ray powder diffraction patterns at high pressure and high temperature were collected at beamline 12.2.2 at the Advanced Light Source at the Lawrence Berkeley National - Laboratory using an X-ray wavelength of  $\lambda = 0.5166\text{\AA}$  (24 keV) and  $\lambda = 0.4969\text{\AA}$  (25 keV) for the silver iodide and San Carlos olivine experiments, respectively. The X-ray energy for the AgI was lowered to 24 keV to be at a safe distance from the Ag-K- $\alpha$ -absorption edge. At each spatial position, X-ray diffraction patterns were taken both before and during the IR laser heating to yield ambient and heated diffraction patterns. The X-ray beam size was 10  $\mu\text{m}$ . Patterns were collected with exposure times of 30 sec on a MAR3450 image plate. The detector distance and orientation were calibrated using a CeO<sub>2</sub> standard at the sample position.

## 1.3 Laser heating and temperature measurement

Laser heating of the LHDAC was conducted using a 1090 nm IR fiber laser system [Kunz *et al.*, 2018], with a beam size of 30  $\mu\text{m}$  FWHM in diameter. The silver iodide sample was heated with 0.9 – 1.0W in both the upstream and downstream directions. The San Carlos olivine sample was heated with powers of 2.5 – 3.2W upstream and 4.5 – 5.7W downstream. To probe the sample across the hot spot, the sample had to be moved relative to the stationary X-ray beam, and with it, the laser hot spot which in turn was kept centered on the gasket hole (see S.I. Figure 1).



S.I. Figure 1: x-y cross section of the LHDAC as seen along the X-ray path. (A) X-ray beam positions (blue) across the diameter of the sample chamber. Note that the laser beam (red) is constantly centered at the origin of the sample space. (B) powdered sample

The center of the gasket hole served as the reference for positioning the laser hot spot. As a result, this procedure created an individual hot spot for every diffraction measurement. The laser heating set-up on beamline 12.2.2 [Kunz *et al.*, 2018] allows for quasi real-time temperature mapping of the sample chamber during a heating event. Temperatures were measured using the double sided spectroradiometric pyrometry set up on beamline 12.2.2, which employs a modified peak scaling approach [Rainey and Kavner, 2014]. This approach avoids the notorious chromatic aberration artifacts and also produces full absolute temperature maps in real time, thus enabling the spatial mapping of the thermal pressure effects presented here.

The pyrometry setup produces upstream and downstream  $74\mu\text{m} \times 74\mu\text{m}$  square temperature maps centered at the peak of the laser hotspot. As a result, radial temperature readings from the center of the sample exist from 0 to  $37\mu\text{m}$  for the full azimuthal range, but disregarding radial completeness, temperature data exist from 0 to  $52.3\mu\text{m}$  from the center. We plotted the upstream and downstream temperatures against radial distance by averaging the temperatures of pixels with the same Euclidian distance (within floating point error) from the center of the  $74\mu\text{m} \times 74\mu\text{m}$  temperature maps. The upstream and downstream graphs were averaged to produce an average temperature vs. radial distance plot.

Due to the large thermal conductivity of the diamond anvils, it has been shown that at the diamond/sample interface, the sample has a temperature close to room temperature [Kiefer and Duffy, 2005]. To construct the temperatures between  $52.3\mu\text{m}$  and  $80\mu\text{m}$  (the sample edge), we use a simple linear decrease between the points at  $(44.5\mu\text{m}, \text{avg}([T_{37\mu\text{m}}, T_{52.3\mu\text{m}}]))$  and  $(80\mu\text{m}, 298\text{K})$ . To construct the first point of the linear decrease, we considered the temperature points between  $37\mu\text{m}$  and  $52.3\mu\text{m}$  because 360-degree azimuthal averaging is only possible between 0 and  $37\mu\text{m}$ . The average

distance and temperature of the points between 37 $\mu\text{m}$  and 52.3 $\mu\text{m}$  gives us the starting point for the linear decrease.

The average beam temperatures of sections centered between 0 and 47.3 $\mu\text{m}$  (52.3 $\mu\text{m}$  – 5 $\mu\text{m}$ ) was obtained by averaging the corresponding 10 $\mu\text{m}$  section (our beam size) of the average temperature vs. radial distance graphs. Average beam temperatures of sections centered between 52.3 $\mu\text{m}$  and 80 $\mu\text{m}$  were obtained by taking the average temperature-value of the linear decrease over the corresponding 10 $\mu\text{m}$  radial section. The thus obtained experimental temperature spots were then fit with a Gaussian function (S.I. Table 1).

**S.I. Table 1: Constants derived from a fit of a Gaussian function (  $T(r)=y_0+(A/(w\sqrt{\pi/2}))\exp(-2((x-x_c)/w)^2)$  ) to the temperature data.**

	<b>Agl</b>	<b>San Carlos Olivine</b>
<b>Y<sub>0</sub></b>	<b>341( 39)</b>	<b>356(37)</b>
<b>x<sub>c</sub></b>	<b>1.84 ± 1.42</b>	<b>-0.11 ± 0.84</b>
<b>w</b>	<b>50.3 ± 3.7</b>	<b>54.7 ± 2.7</b>
<b>A</b>	<b>642377 ± 60777</b>	<b>818137 ± 57077</b>

#### 1.4 Pressure Determination

For computational simplicity, we combine the Murnaghan Equation [Murnaghan, 1951] with the first order equation of thermal expansion through EosFit7 GUI [Angel *et al.*, 2014] for the PVT EOS (Equation 1).

**Equation 1**

$$P = \frac{K_0(1 + \alpha\Delta T)^{-\delta}}{K'} \left( \left( \frac{V_P}{V_0(1 + \alpha\Delta T)} \right)^{-K'} - 1 \right)$$

Within the pressure range and volumetric strains that we probe, the Murnaghan equation is expected to provide a representation of the pressure-volume behavior of these materials that is comparable in accuracy to other, harder to invert finite strain equations of state. The expanded Murnaghan equation (Equation 1) requires observable input values for the initial ( $V_0$ , before heating) and final ( $V_P$ , during heating) sample unit cell volumes, and the temperature ( $\Delta T$ ) experienced by the probed sample volume, together with the physical constants  $K_0$ ,  $K'$ ,  $\alpha$ , and the Anderson-Grüneisen parameter  $\delta$  [Angel *et al.*, 2014; Helffrich and Connolly, 2009]. Note that in this formulation we account for the temperature dependence of the bulk modulus through the Anderson-Grüneisen parameter  $\delta$ , whereas no pressure or temperature dependence of the thermal expansivity  $\alpha$  is included. This simple

formulation of  $\alpha$  reflects that the relative roles of pressure and temperature on this parameter are of opposite sign, and the effect of modest variations in thermal expansion on volume are dwarfed by the pressure effects observed. With  $V_0$  and  $V_P$  determined using the unit cell parameters from before and during the laser-heating, and  $\Delta T$  determined from the temperature map produced by the pyrometry set up on beamline 12.2.2, Equation 1 yields the total pressure at every position of the X-ray/sample transect (S.I. Figure 1). To obtain the thermal pressure component  $P_{th}$ , we subtract the pressure obtained through Equation 1 at the corresponding position prior to the heating from that calculated at high temperatures (i.e. we subtract the pressure applied by the diamonds at ambient temperature).

Scattering intensity versus  $2\theta$  plots were obtained by azimuthal integration of the 2-dimensional powder diffraction patterns using DIOPTAS [Prescher and Prakapenka, 2015]. From the intensity versus  $2\theta$  plots for the silver iodide sample, lattice spacings with Miller indices (200), (220), (311), (222), (400), (420), and (422) were used to refine the unit-cell parameters of silver iodide's cubic crystal structure. From the intensity versus  $2\theta$  plots for the San Carlos olivine, lattice spacings with Miller indices (020), (021), (101), (002), (130), (131), (112), and (211) were analyzed using Celref 3 [Laugier and Bochu, 2002] to yield orthorhombic unit-cell parameters.

## 2 Model Construction

We limit our examination to the thermal pressure arising due to restrictions on the total volume. The construction of our model is as follows:

We reduce the sample chamber to a circular geometry, which we can then partition with the shell differential element. Consider the thermal pressure that arises at the differential element  $r$  (i.e. the region in the radial interval  $[r - dr, r + dr]$ ). Considering this element consequently divides the entire sample into two regions: the interior – the region within the radial interval  $[0, r - dr]$ , and the exterior – the region within the radial interval  $[r + dr, b]$  (where  $b$  is the radius of the entire sample).

Predicated by Heinz [1990], we estimate the temperature distribution with a Gaussian curve. As such, when we move farther away from the center of the sample, the temperature decreases. Thus, the thermal expansion of the interior region  $[0, r - dr]$  occurs at a greater magnitude than that of the exterior region  $[r + dr, b]$ . If we hold the volume of the interior region constant, thermal pressure arises to counteract this thermal expansion according to the restriction. Similarly, holding the volume of the exterior region constant results in a smaller thermal pressure than that of the interior. Doing so lets us think of the  $r$ -shell as being incompressible – which translates to an infinite shear strength analogy. With this construction, the  $r$ -shell experiences a greater thermal pressure from the thermal expansion of the interior volume (which points radially outwards at the boundary  $r - dr$ ) than the thermal pressure it experiences from the exterior (which points radially inwards at the boundary  $r + dr$ ). Of course, in reality as  $dr \rightarrow 0$ , the greater interior thermal pressure would cause the interior volume to expand and thus equilibrate with the outer volume. However, modeling thermal pressure by isochorically restricting the interior volume represents a good upper bound.

With this framework in mind, we can derive a mathematical model. As mentioned above, we use a Gaussian curve to model the temperature distribution of the heated sample (Equation 2).

### Equation 2

$$T(x) = T_0 + \left( \frac{A}{w\sqrt{\pi/2}} \right) \exp\left(-2 \left( \frac{x - x_c}{w} \right)^2\right)$$

Note that Equation 2 is the area version of the Gaussian Equation. Most are familiar with the expression of the Gaussian as a function of the standard deviation ( $\sigma$ ) and mean ( $\mu$ ), i.e.

### Equation 3

$$g(x) = \frac{1}{\sigma\sqrt{2\pi}} e^{-\frac{1}{2}\left(\frac{x-\mu}{\sigma}\right)^2}$$

In Equation 2,  $x_c$  denotes the center of the curve (i.e. at  $x_c$ ,  $T(x_c)$  has its maximum),  $A$  denotes the area under the curve on the interval  $[x_c - \sigma, x_c + \sigma]$ , and  $w$  denotes the width of the curve on the interval  $[x_c - \sigma, x_c + \sigma]$  which is  $2\sigma$ . For conversions between  $w$  and common Gaussian parameters, see S.I. Table 2.

S.I. Table 2: Conversion matrix between different forms of Gaussian functions

$\sigma, w$	$\sigma = w/2$
FWHM, $w$	FWHM = $w\sqrt{2 \cdot \ln(2)}$
Height of the curve ( $y_c - y_0$ )	Height = $\frac{A}{w \cdot \sqrt{\pi/2}}$

Using the area version of the Gaussian function lets us fit our temperature data with the Levenberg-Marquardt iteration algorithm. With Temperature expressed as a function of radius, we can express the thermal expansion coefficient and the bulk modulus as functions of temperature. For the thermal expansion coefficient, we use Equation 4.

### Equation 4

$$\alpha(r) = \alpha_0 + \alpha_1 T(r)$$

For the bulk modulus, we introduce the Anderson-Grüneisen parameter to link compressibility with thermal expansion (Equation 5).

### Equation 5

$$K(r) = K_0 (1 + \alpha(r)\Delta T(r))^{-\delta}$$

In the following derivation of the bulk modulus as a function of radius,  $dV_0$  represents the volume of the unheated shell (i.e. the radial interval  $[r - dr, r + dr]$ ) and  $dV_T$  represents the thermal expansion of  $dV_0$  under unconstrained conditions

$$K(dV_T) = K_0 \left( \frac{dV_0}{dV_T} \right)^\delta$$

$$K(r) = K_0 \left( \frac{dV_0}{dV_0(1 + \alpha(r)\Delta T(r))} \right)^\delta$$

Per the temperature curve, at a given  $r$ -shell, the interior region expands to some heated volume, and the sum of the thermal expansion of the heated interior shells (i.e.  $\int_0^r dV_T$ ) is pressurized to match the isochoric assumption of the interior volume (i.e.  $\int_0^r dV_P = \pi r^2$ ) (Equation 6 & Equation 7). We employ the thermal expansion equation to represent the volumetric expansion of each interior shell (i.e.  $dV_T = dV_0(1 + \alpha(r)\Delta T(r))$ ), and we use the Murnaghan equation (Equation 1) to model the pressure needed to compress the sum of the heated volumes to adhere to the isochoric restriction (Equation 8).

Equation 6

$$dV_P = dV_T \left( 1 + \frac{K'}{K} P \right)^{-\frac{1}{K'}}$$

Equation 7

$$\pi r^2 = \int_r^0 dV_T \left( 1 + \frac{K'}{K} P \right)^{-\frac{1}{K'}}$$

Equation 8

$$\pi r^2 = \int_0^r 2\pi x dx (1 + a(x)T(x)) \left( 1 + \frac{K'}{K(x)} P_{th} \right)^{-\frac{1}{K'}}$$

Thus, Equation 8 presents an upper bound for the thermal pressure that arises at a radial distance  $r$ . Note that due to the steepness of the Gaussian temperature curve in our experiments, the thermal pressure of the interior region dominates the thermal pressure contribution at a given radius, so taking our upper bound results in a good estimate for real thermal pressure.

3 Thermal pressure in isochorically heated volume is equal to  $\alpha K dT$ :

Thermal pressure in a fully constrained volume heated to temperature T is by definition given as Equation 9.

Equation 9

$$P_{th} = \left(\frac{\partial P}{\partial T}\right)_V dT$$

This can be rewritten using the chain rule as Equation 10.

Equation 10

$$\left(\frac{\partial P}{\partial T}\right)_V = \left(\frac{\partial P}{\partial V}\right)_T \cdot \left(\frac{\partial V}{\partial T}\right)_P$$

Since by definition  $\left(\frac{\partial P}{\partial V}\right)_T = K_T$  and  $\left(\frac{\partial V}{\partial T}\right)_P = \alpha_P$ , it follows that in the thermodynamic limit thermal pressure.

$$\left(\frac{\partial P}{\partial T}\right)_V dT = K_T \alpha_P dT$$

Anderson, O. L. (1997), The volume dependence of thermal pressure in solids, *Journal of Physics and Chemistry of solids*, 58(2), 335-343.

Angel, R. J., M. Alvaro, and J. Gonzalez-Platas (2014), EosFit7c and a Fortran module (library) for equation of state calculations, *Zeitschrift für Kristallographie-Crystalline Materials*, 229(5), 405-419.

Chauhan, R., and C. Singh (2007), Equation of state and thermal expansivity of NaCl under high pressure and high temperature, *Physica B: Condensed Matter*, 387(1-2), 352-357.

Heinz, D. L. (1990), Thermal pressure in the laser-heated diamond anvil cell, *Geophysical Research Letters*, 17(8), 1161-1164.

Helffrich, G., and J. Connolly (2009), Physical contradictions and remedies using simple polythermal equations of state, *American Mineralogist*, 94(11-12), 1616-1619.

Hull, S., and D. Keen (1999), Pressure-induced phase transitions in AgCl, AgBr, and AgI, *Physical Review B*, 59(2), 750.

Kantor, I., V. Prakapenka, A. Kantor, P. Dera, A. Kurnosov, S. Sinogeikin, N. Dubrovinskaia, and L. Dubrovinsky (2012), BX90: A new diamond anvil cell design for X-ray diffraction and optical measurements, *Review of Scientific Instruments*, 83(12), 125102.

Kiefer, B., and T. S. Duffy (2005), Finite element simulations of the laser-heated diamond-anvil cell, *Journal of Applied Physics*, 97(11), 114902.

Kunz, M., J. Yan, E. Cornell, E. E. Domning, C. E. Yen, A. Doran, C. M. Beavers, A. Treger, Q. Williams, and A. A. MacDowell (2018), Implementation and application of the peak scaling method for temperature measurement in the laser heated diamond anvil cell, *Review of Scientific Instruments*, 89(8), 083903.

Laugier, J., and B. Bochu (2002), CELREF V3: Cell parameters refinement program from powder diffraction diagram. Laboratoire des Matériaux et du Génie Physique, Institut National Polytechnique de Grenoble, France, edited.

Liu, W., J. Kung, and B. Li (2005), Elasticity of San Carlos olivine to 8 GPa and 1073 K, *Geophysical Research Letters*, 32(16).

Liu, W., and B. Li (2006), Thermal equation of state of  $(\text{Mg}_{0.9}\text{Fe}_{0.1})_2\text{SiO}_4$  olivine, *Physics of the Earth and Planetary Interiors*, 157(3-4), 188-195.

Manga, M., and R. Jeanloz (1996), Axial temperature gradients in dielectric samples in the laser-heated diamond cell, *Geophysical research letters*, 23(14), 1845-1848.

Mao, H., J.-A. Xu, and P. Bell (1986), Calibration of the ruby pressure gauge to 800 kbar under quasi-hydrostatic conditions, *Journal of Geophysical Research: Solid Earth*, 91(B5), 4673-4676.

Murnaghan, F. D. (1951), *Finite deformation of an elastic solid*, John Wiley & Sons.

Prescher, C., and V. B. Prakapenka (2015), DIOPTAS: a program for reduction of two-dimensional X-ray diffraction data and data exploration, *High Pressure Research*, 35(3), 223-230.

Rainey, E., and A. Kavner (2014), Peak scaling method to measure temperatures in the laser-heated diamond anvil cell and application to the thermal conductivity of MgO, *Journal of Geophysical Research: Solid Earth*, 119(11), 8154-8170.